An efficient shape-based procedure for strain hardening identification in the post-necking phase

Mechanics of Materials 196 (2024) 105066

Contents lists available at ScienceDirect

Mechanics of Materials

journal homepage: www.elsevier.com/locate/mechmat

Research paper

An efficient shape-based procedure for strain hardening identification in the post-necking phase

Marta Beltramo *, Martina Scapin, Lorenzo Peroni

Politecnico di Torino, Department of Mechanical and Aerospace Engineering, Corso Duca Degli Abruzzi, 24, 10129, Turin Italy

ARTICLE INFO

Keywords:
Necking
Finite element modeling
Strain hardening model identification
Specimen deformed shape
Database

ABSTRACT

Nowadays, finite element (FE) codes are increasingly employed for simulating large deformation problems. Thus, to reliably represent the strain hardening behavior, a proper calibration of constitutive laws is essential. Focusing on tensile tests, the main issue with ductile metals is necking occurrence, because of the consequent triaxiality and non-uniformity of the strain and stress states. Over the past decades many strain hardening identification approaches have been proposed. Among them, FE-based inverse methods are widely used, but computationally expensive and time consuming. Hence, the authors propose an efficient method which exploits a database for relating the plastic flow rule and the specimen necking profile. The explicit solver of the nonlinear FE code LS-DYNA was used to build the database, whose size could be limited thanks to physical considerations. The developed methodology was applied to experimental quasi-static tensile tests performed on different metals. The predicted hardening laws showed good agreement with those identified with FE-based inverse methods, thus verifying the applicability of the proposed strategy. This study paves the way for machine learning tools having as main input the necking shape: indeed, the present work suggests their feasibility and provides insights into how to establish datasets for a proper and efficient training.

1. Introduction

Nowadays, Finite Element (FE) methods are widely used for studying loading conditions in which large strains are involved (for example, metal forming, dynamic impact processes, energy absorbers, and ductile fracture analysis). It is essential that the material properties used in such FE analyses properly represent the material response, so that reliable results could be obtained.

This highlights the importance of adequately calibrating strain hardening models starting from experimental data. To this aim, a wide variety of tests could be performed: from standard tests, like tensile and compression ones, to more complex tests, such as the bulge test (Rossi et al., 2022) or other tests properly designed to generate multiaxial stress states (Zhang et al., 2021; Li et al., 2021; Yu et al., 2022). Then, different identification strategies can be applied, also depending on the mechanical test chosen. Among all the possible tests, the authors decided to focus on the tensile test because of the ease of execution, the uniaxiality of the force, the possibility to quite easily investigate the effect of temperature, strain-rate, ductile damage, etc. Of course, as all the other possible tests, it has its own drawbacks and limitations, mainly the onset of necking in ductile materials. A literature review of the existing identification methods that deal with this phenomenon is presented in Section 1.1.

During a tensile test, before necking onset, a dog-bone specimen can be assumed to undergo (within its gauge length) a uniaxial and uniform stress state. Therefore, the equivalent (Von Mises) stress σ_{eq} coincides with the axial stress σ_a, and the same holds for the strain (if elastic deformation could be considered negligible with respect to plastic deformation):

$$\sigma_{eq} = \sigma_a;\ \varepsilon_{\mathrm{eq}} = \varepsilon_a. \tag{1}$$

Hence, it is possible to translate the engineering stress $s = F/A_0$ and strain $e = \Delta L/L_0$ (being A_0 the initial cross-sectional area and L_0 the gauge length) into σ_{eq} and ε_{eq}, by reasonably assuming that in metals plastic deformation is a constant volume transformation:

$$\sigma_{eq} = s(1+e);\ \varepsilon_{eq} = \ln(1+e). \tag{2}$$

Conversely, this direct conversion of engineering data to material properties is not possible after the necking onset. The deformation localizes in a limited portion of the specimen and the consequent peculiar

* Corresponding author.
E-mail address: marta.beltramo@polito.it (M. Beltramo).

https://doi.org/10.1016/j.mechmat.2024.105066
Received 22 January 2024; Received in revised form 1 April 2024; Accepted 5 June 2024
Available online 19 June 2024

shape of the specimen causes the stress state to become triaxial and the strain and stress states to lose uniformity (as shown in Fig. 1). However, if the triaxiality and non-uniformity are properly taken into account, the tensile test data can still be used, even after instability, to characterize the material behavior up to larger strains.

As already stated, the different post-necking identification strategies proposed in the last decades are described in Section 1.1. Moreover, approaches that have recently aroused interest are Machine Learning (ML) algorithms, boosted by the need for more time-efficient methods together with the availability of an increasing amount of material data. In general, ML refers to those tools for learning (i.e., making predictions and decisions) from large datasets. In the field of mechanics of materials, these approaches have been used to predict the constitutive parameters starting from experimental measurements. Practically, a metamodel is trained to learn relationships between a set of inputs (e.g., data from tensile tests) and the corresponding set of outputs (e.g., material parameters), thanks to already available data. Input data are usually the force-displacement curve (Koch and Haufe, 2019; Meißner et al., 2020; Marques et al., 2022) or the load history together with the geometry and the strain fields from a region of the sample (Guo et al., 2021).

Although the developed metamodel can be used to quickly predict material parameters directly from experimental data, the training phase could be computationally expensive. Moreover, to properly train the metamodel an adequate dataset must be established (Marques et al., 2022). In this sense, the possibility of using datasets from simulations appears promising, as demonstrated in (Koch and Haufe, 2019; Meißner et al., 2020, 2022; Guo et al., 2021). Of course, suitable material parameters may be found for real experiments as long as the actual material can be accurately described by the predefined hardening rule used in the simulations (Koch and Haufe, 2019). To overcome this issue, larger datasets could be used to account for different possible hardening behaviors; however, this implies higher computational effort for building the datasets and for training the metamodel. In addition, most ML algorithms are at present treated as black boxes, as observed in (Liu et al., 2017; Stoll and Benner, 2021). Consequently, it is generally difficult to strictly control and understand the operations performed within such algorithms. Researchers are working on finding simple, reduced, and interpretable models (Wagner and Rondinelli, 2016; Karniadakis et al., 2021) to address the lack of understandability that has been recognized as one of the major criticisms of ML tools in science (Stoll and Benner, 2021; Schmidt et al., 2019).

This paper investigates the applicability of a database for identifying strain hardening behavior during the post-necking phase, starting from the necking profile. On one hand, to the best of the authors' knowledge, ML approaches using the necking shape as input data have not yet been developed, despite the advantages of shape-based procedures shown in (Peroni and Scapin, 2018; Beltramo et al., 2023). On the other hand, given the concern about the intelligibility of ML tools and the importance of establishing an adequate dataset, the authors believe that conducting a preparatory study is fundamental. This study would enable an efficient and informed implementation of the ML algorithm in subsequent works.

Therefore, instead of using a metamodel to establish a connection between experimental necking shape and post-necking strain hardening behavior, this study proposes a method that simply searches for the best solution within a database (numerically generated). In this way, it evaluates the applicability of a database collecting many necking deformed shapes for identifying strain hardening behavior during the post-necking phase. In addition, some physical aspects are considered to limit the size of the database. Looking ahead, these considerations would allow to efficiently establish a proper dataset for training the metamodel of a ML algorithm. The focus of this study is solely on materials and/or test conditions where the effects of anisotropy, temperature and strain-rate can be considered negligible.

As mentioned earlier, Section 1.1 provides a review of various post-necking identification strategies, to connect the present study to current and previous research. Section 2 explains the key concepts at the basis of the proposed methodology, whereas Section 3 focuses on more practical aspects of the procedure. Finally, the adaptability to different hardening behaviors was evaluated by applying it to experimental tests performed on different metallic materials. The results are reported and discussed in Section 4 in comparison with the results obtained by using analytical and iterative numerical methods.

1.1. Post-necking strain hardening identification methods

Being able to exploit post-necking data is essential especially for almost perfectly plastic materials which reach the instability condition soon after yielding. Moreover, even if for other materials a first estimate of the post-necking behavior could be obtained by extrapolating the mathematical model that fits the pre-necking law, the accuracy of the predictions would not be guaranteed (Tu et al., 2020; Coppieters et al.,

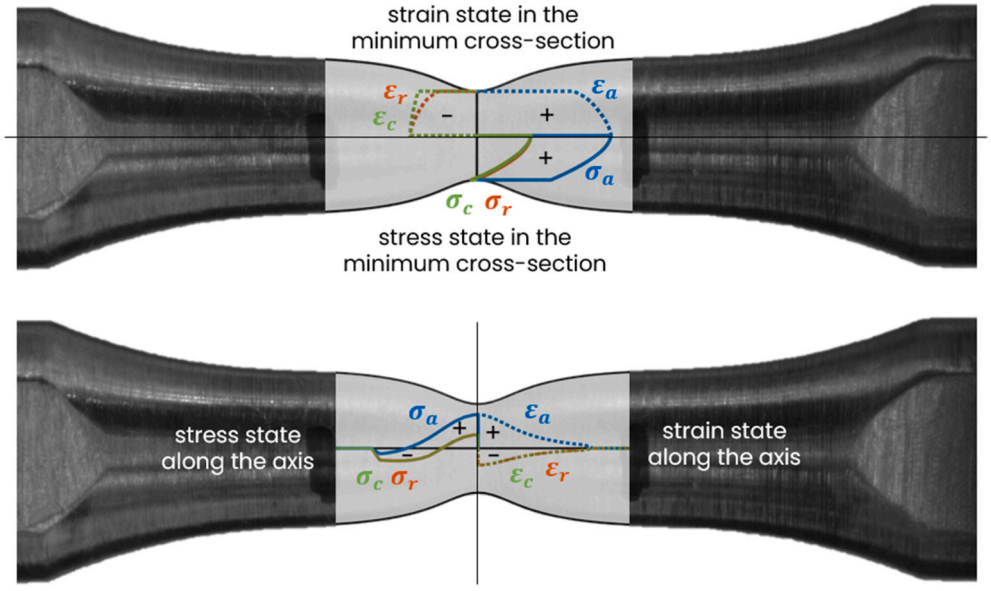

Fig. 1. Stress and strain distributions in the minimum cross section (on the top) and along the longitudinal axis (on the bottom) of a cylindrical dog-bone specimen. Subscripts *a*, *r*, and *c* stand for axial, radial and circumferential components respectively.

2011; Gupta and Singh, 2021; Zhu et al., 2022). Therefore, over the past decades many efforts have been devoted to deal with the necking phenomenon.

The most popular correction formula proposed by Bridgman (1952) belongs to analytical methods and is based on the neck geometry (i.e., the curvature and the minimum radius). More specifically, to obtain the equivalent stress–strain curve $\sigma_{eq} - \varepsilon_{eq}$ of isotropic cylindrical specimens, he proposed the following relationships:

$$\varepsilon_{eq} = 2 \ln \frac{r_0}{r}, \tag{3}$$

$$\sigma_{eq} = \frac{F/(\pi r^2)}{\left(1 + \frac{2R}{r}\right) \ln\left(1 + \frac{r}{2R}\right)}, \tag{4}$$

being r the current minimum radius, r_0 the initial radius and R the radius of curvature at the center of the neck.

Despite being widely used, such method may not be accurate at large strains, as it was found by many researchers (La Rosa et al., 2003; Murata et al., 2018). La Rosa et al. (2003) showed that the error of Bridgman's correction ranges between 3% up to more than 10%. The error could be mainly attributed to the assumption of uniform distribution of the equivalent stress and equivalent strain in the specimen minimum cross-section (Mirone, 2004; Mirone and Corallo, 2010). In the scientific literature it is possible to find several similar analytical solutions, which were proposed to provide more accurate results (Gromada et al., 2011). However, as stated by Tu et al. (2020), these methods, despite providing acceptable results for hardening materials, fail to provide accurate results for perfectly plastic materials (Gromada et al., 2011).

In addition, other methods propose employing numerical investigations to derive correction formulae for converting average axial curves to equivalent curves (Scheider et al., 2004; Li et al., 2019). The main drawback of this class of techniques is that a preselected strain hardening law must be assumed; so, it is not possible to guarantee the accuracy of applying the correction factors found to real materials.

Finally, there are strategies, generally called experimental-numerical iterative approaches, that are based on recursive comparison between measured quantities and the corresponding predicted ones. In particular, these methods search for the optimum hardening behavior, i.e., the one that allows to minimize the difference between certain chosen quantities. For example, FE inverse methods exploit FE simulations to predict the physical quantities that would be compared with the experiment. The quantities iteratively compared may be: the total axial force at a given displacement increment step beyond the maximum force (Zhao et al., 2016; Pham et al., 2021; Yao and Wang, 2022; Zeng and Huo, 2023; Zhang et al., 2023), the specimen deformed shape after the necking onset (Peroni and Scapin, 2018; Beltramo et al., 2023), the shape together with the force time history (Peroni et al., 2015; Scapin et al., 2016, 2019), or the full-field strains in the necking region together with the force time history (Kajberg and Lindkvist, 2004; Gross and Ravi-Chandar, 2015; Zhang et al., 2019). Full-field measurements are also used for other experimental-numerical iterative methods, such as Virtual Field Method or other strategies based on the principle of virtual work (Coppieters et al., 2011, 2016; Kim et al., 2013; Coppieters and Kuwabara, 2014; Fu et al., 2017; Park et al., 2021). In any case, measuring full-field strains requires using Digital Image Correlation (DIC). This implies creating speckle or deposited pattern on the specimen surface and recording it during the test, which could be difficult at very large strains, at high temperature and/or at high strain-rate. For this class of techniques, the issue of assuming a preselected hardening law could be overcome by combining classical flow stress–strain models with each other (Zhang et al., 2023; Defaisse et al., 2018) or by using a piecewise linear relationship between the equivalent stress and equivalent plastic strain (Zeng and Huo, 2023; Coppieters and Kuwabara, 2014; Coppieters et al., 2016; Fu et al., 2017; Park et al., 2021; Defaisse et al., 2018; Dunand and Mohr, 2010, 2011; Wang and Tong, 2015; Marth et al., 2016). However, the consequent increase in model parameters also causes a higher computational effort for the calibration.

Focusing on FE-based inverse methods, it is clear that the computational effort is negatively affected by the fact that all the information that is obtained from one optimization is forgotten when the optimization finishes. If all the attempts that have been done during an optimization were collected into a database, then they would be useful for future analysis.

This is the idea at the basis of the present study. In particular, as anticipated, a database relating the necking deformed external shape to the post-necking hardening law was built. As for the choice of using as input the necking external profile, this is feasible thanks to the correlation that exists between the post-necking plastic flow curve and the necking external shape. Indeed, in Beltramo et al., 2023 the authors showed that it is possible to identify the post-necking material strain hardening behavior (except for the absolute stress value) by looking at a single profile. In that work, a FE-based inverse method was used to identify the plastic flow curve that would lead to a numerical necking profile as close as possible to the experimental one. As shown by Peroni and Scapin (2018) and Beltramo et al. (2023), the great advantage of this approach is that a single image of the specimen can be used for the post-necking characterization. Indeed, this intrinsically contains all the post-necking deformation history without the need to look practically at the time. Moreover, the experimental measurement required is the profile, which can be obtained by digitally analyzing an image to determine just the boundary between the specimen and the background. Such analysis can be conducted more easily than DIC and does not suffer from the loss of focus typical of DIC analysis on cylindrical samples. Furthermore, a speckle on the specimen surface is not needed and this enables the methodology to be extended to high temperature and strain-rate in future research.

2. Proposed methodology and its fundamentals

The present paper aims to evaluate the applicability of a database of necking deformed shapes for identifying strain hardening behavior during the post-necking phase. The identification method proposed to pursue this aim is described hereinafter. For what the pre-necking behavior is concerned, the analytical formula exploiting stress uniaxiality and uniformity are used, whereas the post-necking behavior is determined by searching in a database for the solution which is the closest to the experiment (in terms of necking external profile).

Apparently, to be able to identify every possible behavior, the database should collect all the possible necking shapes that could be generated by all the possible hardening laws. However, some considerations permit to reduce the size of the database: there exists laws that, from the post-necking point of view, are analogous to each other.

First of all, this is the case of hardening laws that have stress values simply scaled one with respect to the other by a coefficient k_σ. Indeed, starting from the same initial geometry, the shape evolution is the same in both cases, whereas the engineering curves are simply scaled by the same coefficient k_σ of the stress. Rigorously, this is true just if the material elastic properties are the same. However, when dealing with metals, the elastic deformations are at least 2 orders of magnitude lower than the plastic strains under analysis. Therefore, being the effect of a different elastic behavior negligible, the previous assertion could still be considered valid.

Secondly, it is important to consider that the necking governing variable is not the total plastic equivalent strain $\varepsilon_{eq,pl}$, but just the amount of plastic equivalent strain after the necking onset $\varepsilon_{eq,pl} - \varepsilon_n$ (being ε_n the equivalent plastic strain at the necking onset). This consideration was at the basis of the analytical methods proposed by Saje et al. (1982), Mirone (2004) and of the inverse method presented by Scheider et al. (2004).

A different ε_n simply changes the current aspect-ratio at the necking

onset, but not how necking will develop. In other words, the post-necking behavior is not affected by the different amount of uniform deformation. Consequently, to evaluate if two laws are equivalent for the post-necking phase it may be meaningful to compare the plastic flow curves by horizontally translating each law in order to remove its own ε_n. For example, the two hardening laws shown as bulk lines in Fig. 2(a), despite being apparently different, actually differ just for the pre-necking part and appear analogous for the post-necking if properly translated horizontally to align their ε_n.

For what the time evolution of the shape is concerned, it should be considered that the radius of the portion far from the neck is almost equal to the radius at the necking onset: this region is the first to undergo unloading, almost immediately after the necking onset. Considering that the different ε_n just affects the size at the necking onset (i.e., the cylinder radius), then the effect of the different ε_n on post-necking deformed shapes is simply a different size. This can be seen from Fig. 2(c): even though the two deformed shapes (in bulk lines) obtained with the two hardening laws (in bulk lines) of Fig. 2(a) appear different, they become overlapped by scaling properly. The coefficient k_g that scales the geometry (both in axial and radial direction) theoretically depends only on ε_n in case of same initial geometry (see Appendix A).

Some experimental evidence in this sense was already presented in Beltramo et al., 2023. There, it was shown that annealed and non-annealed pure copper were characterized by two plastic flow curves that were close to each other if horizontally translated to remove their own plastic equivalent strain at the necking onset. Moreover, the two deformed shapes were very similar, if properly scaled. From a physical point of view, this could be explained considering that annealing reduces the dislocation density and therefore restores the capability of the material to plastically deform.

Finally, it is possible to prove that there exists a relationship even between the two engineering curves of materials with the same post-necking hardening law and initial geometry. This requires more complex considerations that lead to a proper modification of the engineering curves (both in abscissa and ordinate) in order to account for the different ε_n (see Fig. 2(b) and Appendix B).

To sum up, hardening laws that differ from each other just for the pre-necking hardening law and for the scale in stress values are equivalent to each other in terms of necking external shape and engineering curve. This means that a single hardening law, among all these infinite ones, already gives the necessary information, and all the other laws just provide redundant data. Consequently, the size of the database could be reduced. Simultaneously, the previous considerations have implications also for the identification procedure (that will be described in Section 3.2): the necking external profile is linked just to the shape of the post-necking hardening law. Hence, it is not possible to obtain, from the necking profile, the plastic flow curve at strains lower than ε_n (however, it is still possible to use Eq. (2)). Moreover, the necking profile permits to determine only the shape of the post-necking hardening law and not the absolute stress values. Thus, to find the absolute stress values additional information regarding the engineering stress must be taken into account.

3. Practical aspects

This section describes how the database used for the proposed strategy was built and how the identification procedure works. Moreover, its capability of dealing with different sources of error was investigated.

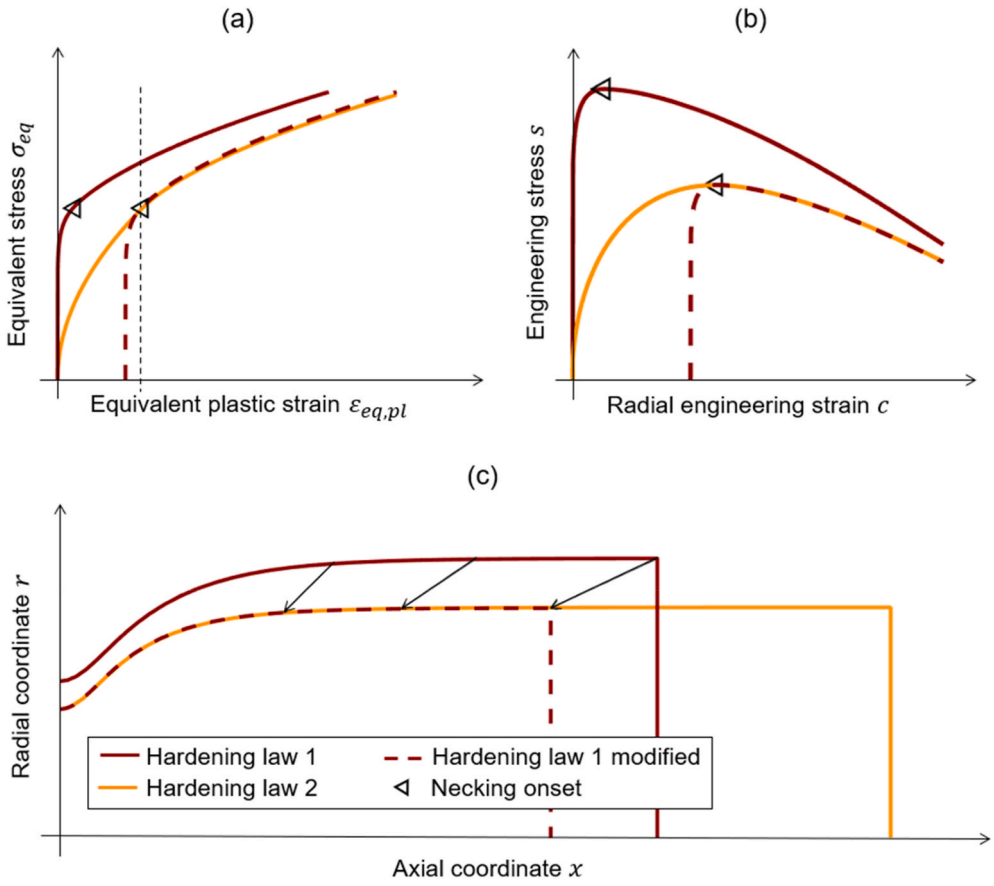

Fig. 2. Results of two tensile tests on cylinders with same initial geometry and made of material with two different hardening laws, called law 1 and law 2 (a). (b) Shows the engineering curves (being the engineering stress $s = F/A_0$ and the radial engineering strain $c = |\Delta R|/R_0$) and (c) shows the deformed shapes. Darker dashed lines are obtained by properly modifying darker bulk lines in order to remove the effect of different ε_n.

3.1. Database construction

The database collects the results (in terms of engineering curve and external profiles at different time instants) of tensile tests on materials with different hardening behaviors. In particular, it was numerically built by running FE simulations of tensile tests with the explicit solver of the commercial FE code Ansys LS-DYNA. Actually, the FE model used was always the same, except for the hardening law that changed from one simulation to another.

Cylindrical specimens with aspect-ratio $L_0/D_0 = 4$ were adopted to avoid introducing any boundary effect, and to improve the generality of the method, so that it could be applicable to specimens with different aspect-ratios. To reduce the computational time of building the database, the cylinder was modeled through axisymmetric shell elements with one integration point. Actually, half of the specimen was considered by applying a symmetry constraint at one end and a prescribed velocity to the other end. For the latter boundary condition, a slow and smoothly varying curve was used so that inertial effects were not introduced.

The adopted mesh was characterized by small elements in the region where necking would develop and coarser elements elsewhere (this was widely used starting from Tvergaard and Needleman, 1984) and mesh size convergence was investigated in order to adequately choose the element size. Elements' initial aspect-ratio was such that, during necking development, a regular element shape was obtained. Nevertheless, simulation results are considered reliable just until element distortion is limited. Finally, elements at the center of the specimen were characterized by a slight reduction of mechanical strength so that necking was triggered exactly there; it was verified that this choice did not affect the results. Equivalently, instead of a reduction of material strength, a geometrical imperfection could be introduced (Tvergaard and Needleman, 1984; Zhang et al., 1999; Roy et al., 2022).

For what the material model is concerned, a series of power-law hardening curves $\sigma_{eq} = K\varepsilon_{eq,pl}^{N}$, obtained by varying a single parameter (N), were used. This was implemented in LS-DYNA via the material card *MAT_015. As explained in Section 2, what actually matters in building the database is considering different shapes of the post-necking hardening law (regardless of the absolute stress values and the pre-necking behavior). In the specific case of a power-law model, varying the hardening exponent is enough to obtain all the possible shapes of the post-necking part of the plastic flow curve. For what the strength coefficient K is concerned, its specific value is not relevant (provided that the ratio K/E is in the typical range of metals), since in the identification procedure this would simply change the stress coefficient k_σ. It may seem that this database would be adequate just for those materials which are well represented by Hollomon or simplified Johnson-Cook hardening models. However, it should be taken into account that only the post-necking part of a power-law model is used to describe the post-necking part of the analyzed material, so the database could even catch saturating behaviors thanks to hardening exponent close to 0. In addition, although the present work considers just a specific hardening model, the proposed method is applicable also to other hardening models, so the database could be properly enriched in order to catch different behaviors.

All the other material properties used in the FE model are fixed to predefined values since they are assumed to have a negligible effect: e.g., the density has no influence since inertia is usually considered a secondary effect, especially in quasi-static tests; Young's modulus and Poisson's ratio regard elastic deformations that are reasonably negligible with respect to the plastic deformations reached in large post-necking phase.

For exemplary reasons, in Fig. 3(a) some of the hardening laws used to build the database are plotted. Despite the laws used for FE simulations were actually $\sigma_{eq} - \varepsilon_{eq,pl}$ curves, the quantities chosen for the abscissa and the ordinate of Fig. 3(a) are different in order to focus the attention just on the shape of the post-necking part. To practically obtain this plot, each curve $\sigma_{eq} - \varepsilon_{eq,pl}$ was horizontally translate backward of its own ε_n and the stress values were normalized with respect to the stress σ_n at the necking onset. As already mentioned, each law was used for simulating a tensile test on a different material. Among all the deformed configurations that were obtained from every simulation and that were collected in the database, just one for each law is shown in Fig. 3(b). The choice was to show, from each virtual test, the configuration characterized by a certain maximum post-necking strain reached on the specimen surface (as an example and without loss of generality, in Fig. 3(b) the case $\max(\varepsilon_{eq,pl}) - \varepsilon_n = 0.8$ was considered). To highlight again just the post-necking behavior, both the axial and the radial coordinate of each profile of Fig. 3(b) were normalized with respect to their own radius r_n at the necking onset. This shows that, despite being all these profiles characterized by the same range of r/r_n, the shape itself is different because of the different post-necking behavior: the lower the hardening rate, the more localized the deformation. Finally, the markers that indicate the same post-necking strain level in Fig. 3(b) are almost horizontally aligned between the different shapes, thus underlining the strong correlation between $\varepsilon_{eq,pl} - \varepsilon_n$ and r/r_n.

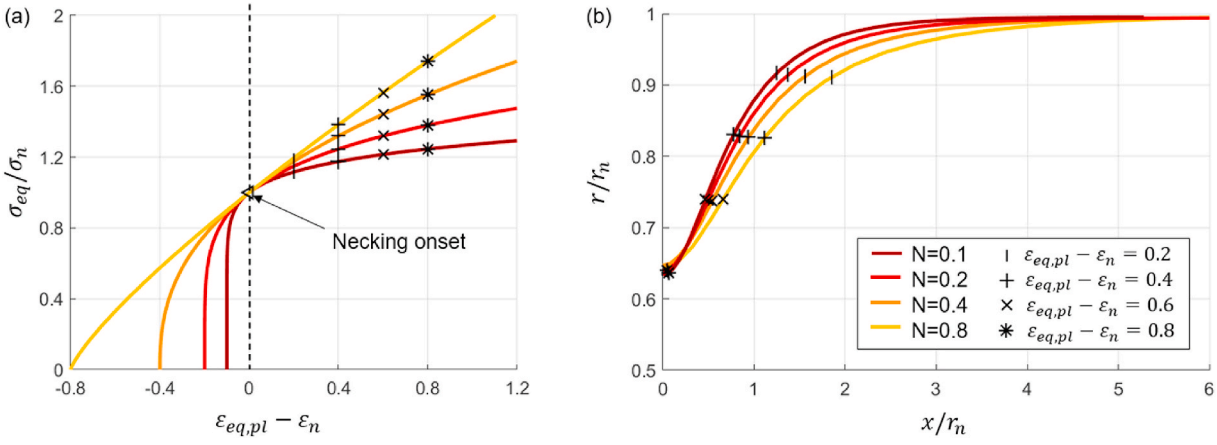

Fig. 3. (a) Some hardening laws $\sigma_{eq} = K\varepsilon_{eq,pl}^{N}$ used to build the database; each curve properly translated backward of its own ε_n and normalized with respect to the stress σ_n at the necking onset. (b) Deformed profiles (one for each hardening law) characterized by the same $\max(\varepsilon_{eq,pl}) - \varepsilon_n = 0.8$; each profile normalized with respect to its own radius r_n at the necking onset; markers are used to indicate the post-necking strain levels along the profile.

3.2. Post-necking identification procedure

In this paragraph the procedure for characterizing the post-necking domain is presented. The fundamental concepts at the basis of the method (explained in Section 2) are briefly summarized hereinafter. The necking profile (regardless of the absolute size) is linked just to the shape of the post-necking hardening law (regardless of the absolute stress values). This implies that the profile could be used to identify the shape of the post-necking hardening law, whereas determining the absolute stress values requires information on the engineering curve. Thus, the experimental data required are the engineering curve (or part of it) and a single necking profile. Given such information, the identification procedure consists of the following steps.

1. The shapes, represented by the data couples (x_{db}, r_{db}), are taken one by one from the database and each one is scaled (both in axial and radial direction) through a coefficient k_g.

   This coefficient, as explained in Appendix A, ideally depends just on $\varepsilon_{n,db}$ of the simulation, ε_n of the experiment, and on the initial specimen diameter (if different). Actually, to deal with unavoidable uncertainties (both numerical and experimental), each profile of the database is optimally scaled, i.e., in order to minimize the difference with the experimental profile itself.
2. For each scaled shape, represented by the data couples $(\widetilde{r}_{db}, \widetilde{x}_{db})$, the distance to the experimental profile is computed in terms of $\| \widetilde{r}_{db} - r_{exp} ||_2$. Of course, just the specimen gauge length (or even a smaller portion) is considered, in order to limit the boundary effects of applying a cylinder database to a dog-bone specimen (this aspect is analyzed further in Section 3.3).
3. The database shape associated with the smallest distance is selected; in Fig. 4(a) it is qualitatively shown (dotted line) in comparison with the experimental one (bulk line). The plastic flow curve of the simulation that led to that shape is the one that, among all those considered, best represents the post-necking plastic flow curve. This is reported in Fig. 4(c) (dotted line), translated horizontally to compensate for the different ε_n.
4. The engineering curve of the selected simulation (properly modified to account for the different ε_n, as explained in Appendix B) is compared with the experimental engineering curve (bulk line in Fig. 4(b)). In this way, it is possible to find the value of the coefficient k_σ that adequately scales the post-necking hardening law. In Fig. 4(b) the engineering curve from the database is plotted both before (dotted line) and after (dashed line) having applied a coefficient k_σ to scale the stress values. The same is done for the plastic flow curve, as shown in Fig. 4(c).

   To compare the experimental engineering curve with the engineering curves of the database, it is necessary to have comparable evaluations of the strain. The traditional longitudinal engineering strain based on the axial elongation is highly dependent on the reference length itself (Rösler et al., 2007). Therefore, the macroscopic quantity chosen to evaluate the strain is the radial (and equivalently hoop) contraction in the minimum cross-section. This will be called radial engineering strain (and for definition coincides with the hoop engineering strain).
5. The identified post-necking law and the pre-necking hardening law (determined through analytical formulae) are properly joined at the necking onset strain ε_n. This point is determined in correspondence of the maximum load, neglecting the delay of the bifurcation with respect to this condition (Hutchinson and Miles, 1974).

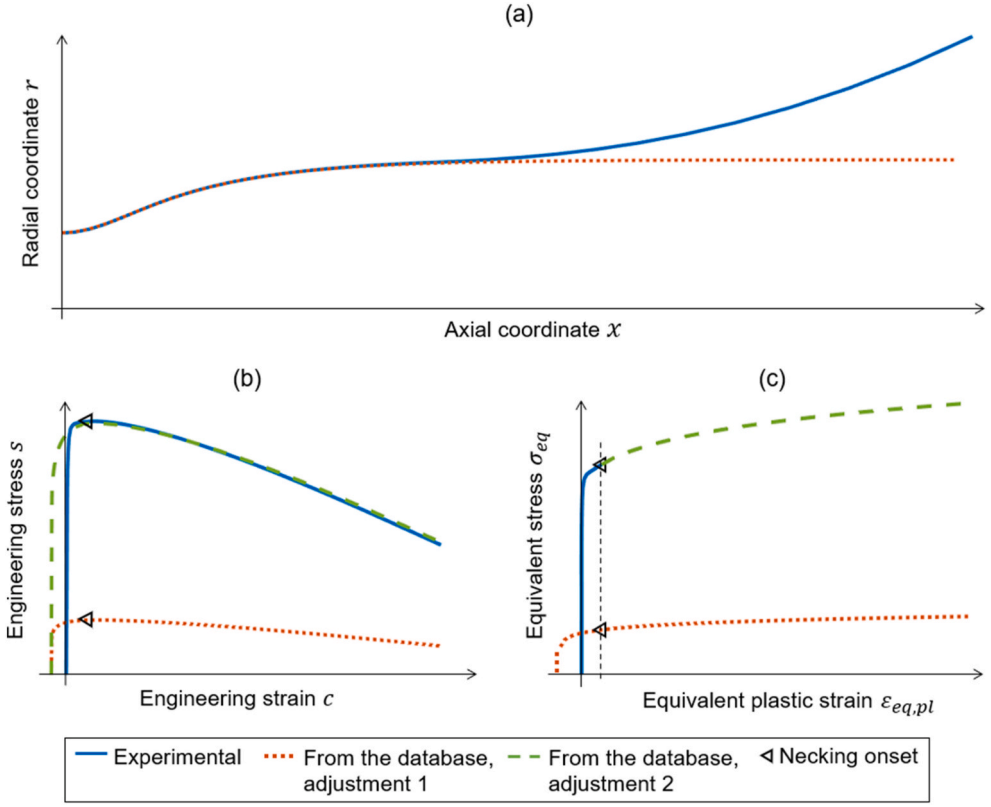

Fig. 4. Steps of the identification procedure in terms of necking shape (a), engineering curve (b) and equivalent curve (c). Adjustment 1 refers to shape, engineering curve (in terms of engineering stress $s = F/A_0$ and radial engineering strain $c = |\Delta R|/R_0$) and hardening law taken from the database and properly adapted to compensate for the different ε_n. Adjustment 2 refers to a further modification of the results of adjustment 1, i.e., the engineering curve and hardening law are properly scaled in stress values.

3.3. Effect of applying a database of cylinder to a dog-bone specimen

A database of cylinders was chosen so that it could be applicable to experimental tests performed on specimens with different aspect-ratios. However, the geometrical difference may have some effects on the identification. Therefore, a numerical study was carried out to evaluate such effects for specimens with different aspect-ratios (see Fig. 5) and made of materials with different hardening behavior.

More specifically, five materials were considered. To ensure that the results depend solely on the different post-necking behaviors, all the materials are characterized by $\varepsilon_n = 0$. The different hardening behaviors are shown in black lines in Fig. 6 and are denoted with capital letters. Each curve is normalized with respect to its own stress at the necking onset. For each of them, five tensile tests were simulated, changing the aspect-ratio L_0/D_0 of the cylindrical dog-bone specimen. The simulated tests were then considered as they were experimental tests, and the post-necking identification procedure described in Section 3.2 was applied to each of the 25 tests.

The table of Fig. 6 collects, for all the tests, the Normalized Root-Mean-Square Errors (NRMSE) of the identified equivalent stress $\widehat{\sigma}_{eq}$ with respect to the reference one σ_{eq} (over the strain range shown in Fig. 6). More specifically, the errors were computed as $\mathrm{RMSE}(\widehat{\sigma}_{eq})/\mathrm{average}(\sigma_{eq})$. It is possible to observe that for each material the slimmer the specimen, the lower the error. This is reasonable because boundary effects decrease for slimmer specimens. The results are also presented in terms of plastic flow curve in the plot of Fig. 6. The gray region represents the maximum error on the identified law for each material. Overall, the results prove that a database of cylinders can be successfully applied to experimental tests on dog-bone specimens.

3.4. Effect of experimental uncertainties in measuring the necking profile

In this study the necking profile is fundamental both for acquiring the deformed shape and for calculating $c = |\Delta R|/R_0$. Thus, it is necessary to test robustness of the approach against errors in the experimental measurement of the profile. For this analysis, to avoid having other sources of error, a reference shape was chosen within the database and a random uniform noise was added. The noisy profile was considered as an experimental measurement and the identification was performed.

Practically, consider the reference external profile to be represented by $\boldsymbol{x}$ and $\boldsymbol{r}$, arrays collecting the x_i and r_i coordinates of different points. To the array $\boldsymbol{r}$ a perturbation $\Delta\boldsymbol{r}$ was added, which represents the noise and contains random scalars drawn from the uniform distribution in the interval $(-\delta/2, \delta/2)$.

As shown in Fig. 7, the resulting profile can be a random one within the gray region around the reference profile. The analysis was conducted with different levels of error, i.e., the amplitude δ of the gray region was varied from a minimum of 10 μm up to a maximum of 100 μm. The table of Fig. 7 reports the NRMSEs for different levels of noise in the measured profile.

It can be seen that uncertainties of about 100 μm on the experimental necking profile may lead to non-negligible errors on the identified law. However, it should be considered that an error of 100 μm corresponds to a very noisy profile (see Fig. 7). Moreover, the threshold for error acceptability depends on the specific engineering application. Thus, overall, the procedure appears sufficiently robust: indeed, searching within the database for the best shape automatically filters the profile against non-physical high-frequency oscillations. This further demonstrates the procedure's capability to find the correct solution.

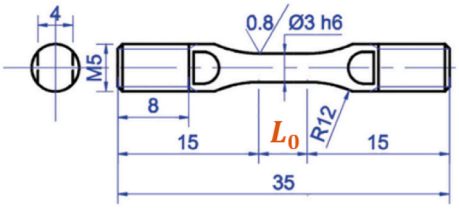

Fig. 5. Sketch of the cylindrical dog-bone specimen used for the numerical analysis by varying the length L_0. Figure adapted from (Scapin et al., 2014).

4. Experimental case studies

The proposed methodology was applied to experimental quasi-static tests conducted on different materials: Al6082-T6, pure copper, and 17-4 PH. As the method is based on the hypothesis of isotropic behavior, the specimen axial-symmetry was firstly verified. For comparative purposes, the identification was also performed with Bridgman's correction and FE-based inverse methods.

4.1. Experimental setup and procedure

Cylindrical dog-bone specimens with threaded ends and characterized by a 3 mm gauge diameter and a 5 mm gauge length were used (see Fig. 5). Tensile tests were performed on a standard electromechanical testing machine, Zwick-Z100, in quasi-static conditions (testing speed of 0.05 mm/s) and at room temperature. The force was measured with a 100 kN load cell, and the deformation of the sample was obtained by digitally analyzing the images captured through a high-resolution camera at 1 fps. More specifically, a PixeLINK PL-B777 camera with a resolution of 2592 × 1944 pixels and equipped with a Tokina Macro 100 F2.8 D camera lens was employed. The setup allowed a resolution of 7 μm/pixel and through digital image analysis (binarization and segmentation of images performed in MATLAB) the time evolution of the external contour of the specimen profile was obtained. This measurement did not suffer from loss of focus: at the beginning of the test, the camera was focused on the plane on which the profile was and, since the profile reasonably remained on the same plane during the whole test, it remained in focus too.

Before the necking onset, each profile could be used for determining the current radius of the sample (by adequately averaging over the gauge length). Thus, the axial stress σ_a and the axial strain ε_a could be computed according to the following relations (under the hypothesis of volume conservation):

$$\sigma_a = \frac{F}{\pi r^2}, \quad \varepsilon_a = 2\ln\left(\frac{r_0}{r}\right). \tag{5}$$

Up to the necking onset, these quantities coincide with σ_{eq} and ε_{eq} (see Eq.(1)). Hence, it was possible to obtain the equivalent plastic strain, so that the pre-necking plastic flow curves were found. Conversely, the post-necking part was identified by applying different approaches: Bridgman's analytical correction (according to Eqs. 3-4), the proposed method, a FE-based inverse method having as target the post-necking engineering curve, and a FE-based inverse method having as target the necking profile (more details could be found in Beltramo et al., 2023).

For the proposed strategy, the database and the procedure described in Section 2 were used. For the two FE-based inverse methods, an optimization was required, and it was implemented on the commercial program Ansys LS-OPT. More specifically, a metamodel-based optimization was chosen and a sequential strategy with domain reduction was adopted. For what the model parametrization is concerned, a single parameter was used because the post-necking law was modeled as the post-necking part of a power-law hardening model. This choice was made to get results comparable with the method proposed in this work.

In all these post-necking identification strategies, the specimen external profiles obtained through digital image analysis were used, as better detailed in the following paragraphs.

To apply Bridgman's correction, the radius and the curvature at the necking center must be evaluated during the whole test. To this aim, for reducing the noise, the ideal symmetry of the deformed sample was

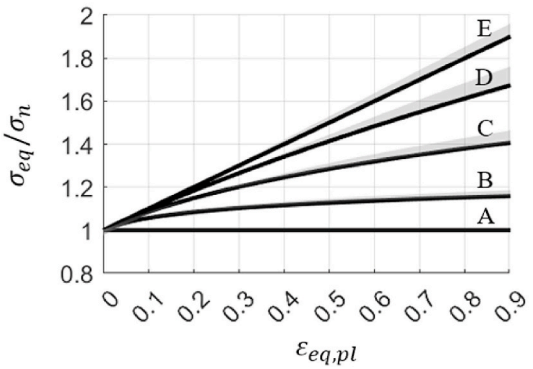

	A	B	C	D	E
$L_0/D_0 = 1$	< 1 %	1.6 %	2.5 %	3.3 %	2.4 %
$L_0/D_0 = 1.5$	< 1 %	1.1 %	1.8 %	2.1 %	1.8 %
$L_0/D_0 = 2$	< 1 %	< 1 %	1.4 %	1.7 %	1.0 %
$L_0/D_0 = 3$	< 1 %	< 1%	< 1 %	1.1 %	< 1 %
$L_0/D_0 = 7$	< 1%	< 1%	< 1 %	< 1%	< 1 %

Fig. 6. Application of the proposed method to dog-bone specimens with different aspect-ratios, made of materials with different hardening behavior (from A to E). The plot shows the reference laws (black lines) and for each of them a gray region representing the maximum error obtained by varying the aspect-ratio. The stresses are normalized with respect to the stress at the necking onset of the corresponding reference law. The table shows the error of the identified law $\widehat{\sigma}_{eq} - \varepsilon_{eq,pl}$ with respect to the reference one $\sigma_{eq} - \varepsilon_{eq,pl}$, evaluated through the normalized root-mean-square error between the stress values $\text{NRMSE} = \text{RMSE}(\widehat{\sigma}_{eq})/\bar{\sigma}_{eq}$.

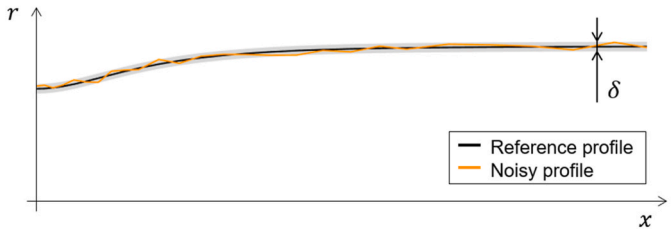

	NRMSE
$\delta = 10\ \mu m$	< 1%
$\delta = 20\ \mu m$	1.4 %
$\delta = 50\ \mu m$	3.7 %
$\delta = 100\ \mu m$	6.7 %

Fig. 7. Application of the proposed methodology to noisy profiles. On the left, a representation of the reference profile and a random profile within the uncertainty region in gray. On the right, error of the identified law $\widehat{\sigma}_{eq} - \varepsilon_{eq,pl}$ with respect to the reference one $\sigma_{eq} - \varepsilon_{eq,pl}$, evaluated through the normalized root-mean-square error between the stress values $\text{NRMSE} = \text{RMSE}(\widehat{\sigma}_{eq})/\bar{\sigma}_{eq}$.

exploited, and a single average semi-profile was determined for each time instant considered. Then each average necking semi-profile was fitted with a polynomial function (as done in La Rosa et al., 2003 and Dunnett et al., 2012 for example) and the curvature was approximated with the curvature of such function in the center of necking.

Conversely, to apply the proposed characterization strategy and the FE-based inverse method having as target the necking profile, it was necessary to choose a single deformed configuration and to consider the specimen profile just at that time instant. As before, to reduce the noise, a single average semi-profile was determined. This semi-profile represented the target of the FE-based inverse method, and the one to be compared with the profiles stored in the database (that are actually semi-profiles).

Finally, the FE-based inverse method having as target the post-necking engineering curve required the time history of the minimum cross-section radius. Indeed, as anticipated in Section 2, the authors chose to evaluate the radial engineering strain through the dimensionless quantity $c = |\Delta R|/R_0$ (ΔR computed at the minimum cross-section in post-necking regime), and this was possible thanks to the images analyzed. To reduce the level of noise in measuring ΔR, non-physical high-frequency oscillations were neglected by applying a moving average filter on the measured profile.

To conclude, since ductile damage (void nucleation, growth, and coalescence) was not considered in any of the previous characterization strategies, it is important that data used for the identification are not significantly affected by this phenomenon. This is why preliminary tests were conducted to ensure that, in the configurations considered, void nucleation and coalescence did not have a relevant effect on the mechanical strength (Tvergaard and Needleman, 1984).

4.2. Experimental results and discussion

The plastic flow curves $\sigma_{eq} - \varepsilon_{eq,pl}$ resulting from the different identification procedures are reported in Fig. 8(a), 9(a), 10(a) for the three different materials. The true curve $\sigma_a - \varepsilon_a$ (according to Eq. 5) are reported too to highlight that, soon after necking, neglecting triaxiality would lead to a considerable error. The laws identified with the database methodology, and shown in this section, could be properly joined with the pre-necking part to ensure the continuity and to guarantee a monotonically decreasing hardening rate.

The laws that should be considered more reliable are those identified with FE-based inverse method because they do not have the simplifying assumptions of Bridgman's theory and of the proposed method. Moreover, FE-based inverse methods allow to easily obtain the maximum strain $\varepsilon_{eq,pl}^{max}$ reached within the specimen at the last deformed configuration analyzed; $\varepsilon_{eq,pl}^{max}$ represents the last point of the hardening law that it is reasonable to consider.

For each material, a small discrepancy between the two FE-based inverse methods can be noticed, but it is not possible to state that one law is better than the other (Beltramo et al., 2023). Thus, both laws are considered for evaluating if the proposed database method, which is far less computationally expensive than FE-based inverse methods, is able to give comparable results. Moreover, for comparison purpose, the hardening law obtained with Bridgman's analytical correction is reported too.

For what Bridgman's correction is concerned, the results for Al6082-T6 in Fig. 8(a) confirm that such method fails to provide reliable results for materials with low hardening rate (Tu et al., 2020; Gromada et al., 2011). Conversely, the results for pure copper and 17–4 in Fig. 9(a) and Fig. 10(a) highlight that the correction is good at low strain levels, but it introduces an increasing error at large strains. Moreover, Bridgman's

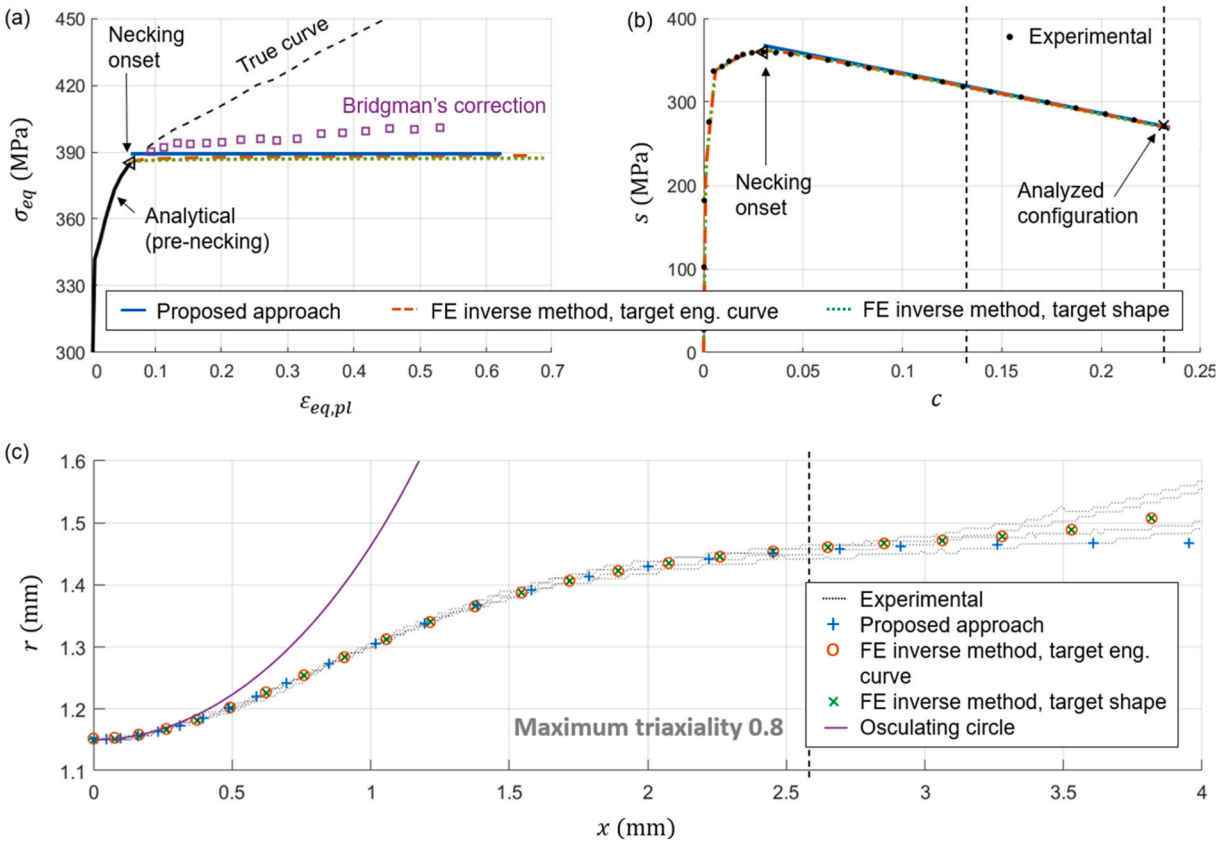

Fig. 8. Experimental results of Al6082-T6, in terms of (a) plastic flow curve, (b) engineering curve (in terms of engineering stress $s = F/A_0$ and radial engineering strain $c = |\Delta R|/R_0$), (c) specimen profile, in comparison with the numerical prediction obtained from different identification strategies.

theory estimates the last point of the hardening law at a strain level lower than the actual $\varepsilon_{eq,pl}^{max}$ because it actually estimates the average value of $\varepsilon_{eq,pl}$ on the minimum cross-section.

These issues appear to be overcome with the proposed method, which is as fast as Bridgman's approach, but does not have any simplifying hypothesis on the stress and strain fields (since it is based on FE results). Furthermore, having in the database also the equivalent plastic strain information, it is possible to estimate $\varepsilon_{eq,pl}^{max}$. This explains why the different plastic flow curves of Fig. 8(a), 9(a), 10(a) are plotted up to different strains.

Overall, the discrepancy of the proposed method with respect to FE-based inverse methods, evaluated as NRMSE on the stress, is 1% for Al6082-T6, 2.5% for pure copper and 2% for 17-4 PH. To better understand the origin of these discrepancies, a comparison in terms of engineering curve and deformed profile is proposed too.

In Fig. 8(b), 9(b), 10(b) the experimental engineering curve $s - c$ is compared with the engineering curve taken from the database. This latter was properly modified to compensate for the different uniform deformation and to take into account the scale factor k_σ of the stress (vertical dashed lines indicate the portion used to determine this coefficient). The engineering curves obtained with FE inverse methodologies are also reported. Of course, the FE-based inverse method having as target the engineering curve is the one that led to the best results, but good results were obtained also with the other strategies. Pure copper is the material in which a higher discrepancy was found. This can be attributed to the fact that a power-law hardening model may not be adequate to represent the material post-necking behavior. This is further highlighted by the comparison of the necking profile, as explained hereinafter.

In Fig. 8(c), 9(c), 10(c) the experimental semi-profiles are compared with the best semi-profile from the database (properly scaled) and the semi-profiles obtained with FE inverse methodologies. Since both FE-based inverse methods used the same FE model, the nodes positions shown in Fig. 8(c), 9(c), 10(c) are coincident if the laws are in good agreement with each other. This is true especially for Al6082-T6 and 17-4 PH, whereas in pure copper a slightly higher difference can be seen (of course the methodology having as target the profile is the one that best predicts it). Again, the discrepancy underlines the limitation of a predefined hardening law. An improvement could be obtained by enriching the database with hardening models different from a power-law.

In Fig. 8(c), 9(c), 10(c), for what the experimental specimen shape is concerned, all four semi-profiles are reported (black dotted lines). In addition, a vertical dashed line highlights the portion considered for the proposed method, for the FE-inverse method having as target the deformed shape, and for fitting the polynomial function when applying Bridgman. On one hand, this allows to verify that, within this portion, it is reasonable to consider an average semi-profile as target, because the discrepancy is small. However, the fact that, for the Al6082-T6 specimen, the neck did not develop in the middle of the specimen may still introduce uncertainties in the identification. On the other hand, the vertical dashed line shows that the portion affected by the shoulders was excluded from the analysis; this is important when applying a cylinder database to dog-bone specimens.

Finally, in Fig. 8(c), 9(c), 10(c) the circle osculating the neck profile (used for Bridgman's correction at that configuration) is shown too, highlighting that Bridgman's approach is based on a local evaluation of the shape. This is probably the cause of the outliers that can be found in the hardening law for pure copper of Fig. 9(a). As well-known, Bridgman's method is sensitive to the technique used to determine the curvature at the necking center. In this sense, the method proposed in this paper takes advantage of not being limited to a local analysis of the necking center (Scapin and Beltramo, 2024).

Overall, the results reported here allow one to verify that the

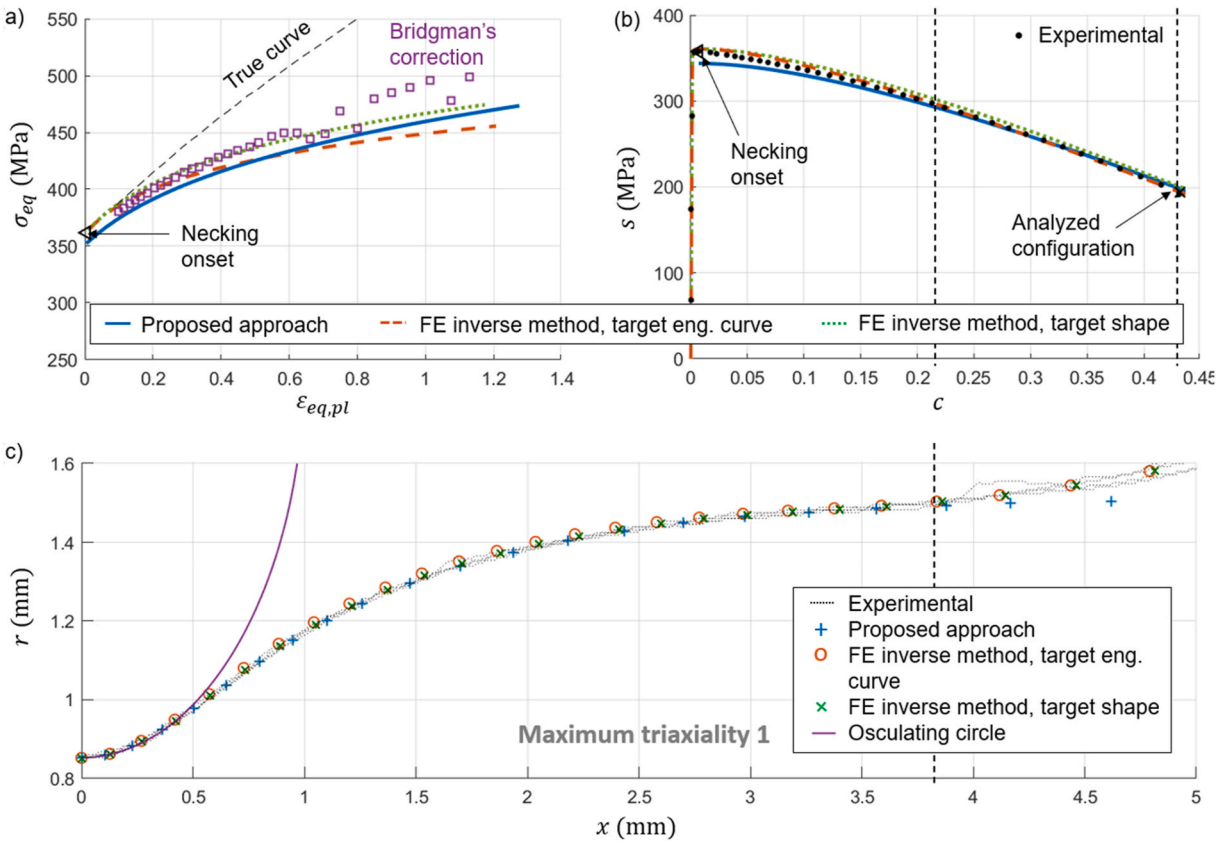

Fig. 9. Experimental results of pure copper, in terms of (a) plastic flow curve, (b) engineering curve (in terms of engineering stress $s = F/A_0$ and radial engineering strain $c = |\Delta R|/R_0$), (c) specimen profile, in comparison with the numerical prediction obtained from different identification strategies.

proposed method is in good agreement with computationally expensive techniques that do not have simplifying hypotheses on the geometry. Meanwhile, the comparison with Bridgman's correction, which is as fast as the proposed method, highlights the advantages of not having assumed specific stress and strain fields and of analyzing a wider portion of the profile (and not only the necking center). Such assertions are valid even for quite different materials as those investigated. Satisfying results have been obtained for a high-strength material showing a conventional static behavior (17-4 PH), but also for the other two materials, which exhibited more peculiar static responses. Al6082-T6 showed an abrupt change of the hardening behavior, with a dramatic reduction of the hardening rate at the necking onset. Pure copper reached the instability condition soon after yielding. These two latter cases are clear examples in which simply extrapolating a hardening law that fits the pre-necking part would lead to considerable errors in the identified equivalent curve.

Moreover, it is worth noting that, even with a database built from a power-law hardening model, it is possible to catch a saturating behavior, as that shown by the aluminum alloy. This is possible because just the post-necking part of a power-law model is used to describe the post-necking part of the analyzed material. Therefore, a hardening exponent close to 0 gives a behavior very close to that of a saturating law.

Finally, the computational effort of the proposed method is much lower than FE-based inverse techniques: it takes just a few seconds to obtain the plastic flow curve. This could be expected, since the major computational effort is in building a database, whereas the characterization consists simply of searching within the database.

5. Conclusions

The purpose of the present work was to evaluate the applicability of a database of necking deformed shapes for identifying strain hardening behavior during the post-necking phase. This aim was pursued through an identification method that consists of searching for the hardening law, already available in a database, which led to the numerical result closest to the experiment (in terms of external deformed profile). A procedure based on the specimen external contour has the great advantage of not requiring DIC analysis, because it is sufficient to determine the boundary between the specimen and the background.

Applying the proposed method to some experimental case studies showed that the algorithm took a few seconds to find a solution in accordance with more computationally expensive techniques. Of course, the proposed strategy would not replace other identification methods when accurately characterizing the material, but it may be used as starting point in order to reduce the computational effort of experimental-numerical iterative methods.

Although the method proposed in this paper can work as an efficient identification strategy on its own, the outcomes of this study will be useful in future works for efficient and informed implementation of ML algorithms having the necking external profile as main input. Indeed, the applicability and the potential of such algorithms was highlighted by the successful application of the proposed method to experimental cases. Satisfying results have been obtained on materials characterized by different behaviors in terms of maximum uniform deformation, resistance, ductility, and hardening rate. Moreover, numerical investigation proved the method's robustness against uncertainties in experimentally measuring the specimen profile.

In addition, the generality of the proposed method, from the geometrical point of view, was highlighted: it was shown that applying a cylinder-database to dog-bone specimens introduces acceptable errors. This observation, together with the physical aspects presented in Section 2, suggest how, in subsequent studies, a proper dataset could be efficiently established for training the metamodel of a ML algorithm. Furthermore, an important outcome of experimental case studies was that a database built with a power-law hardening model was able to

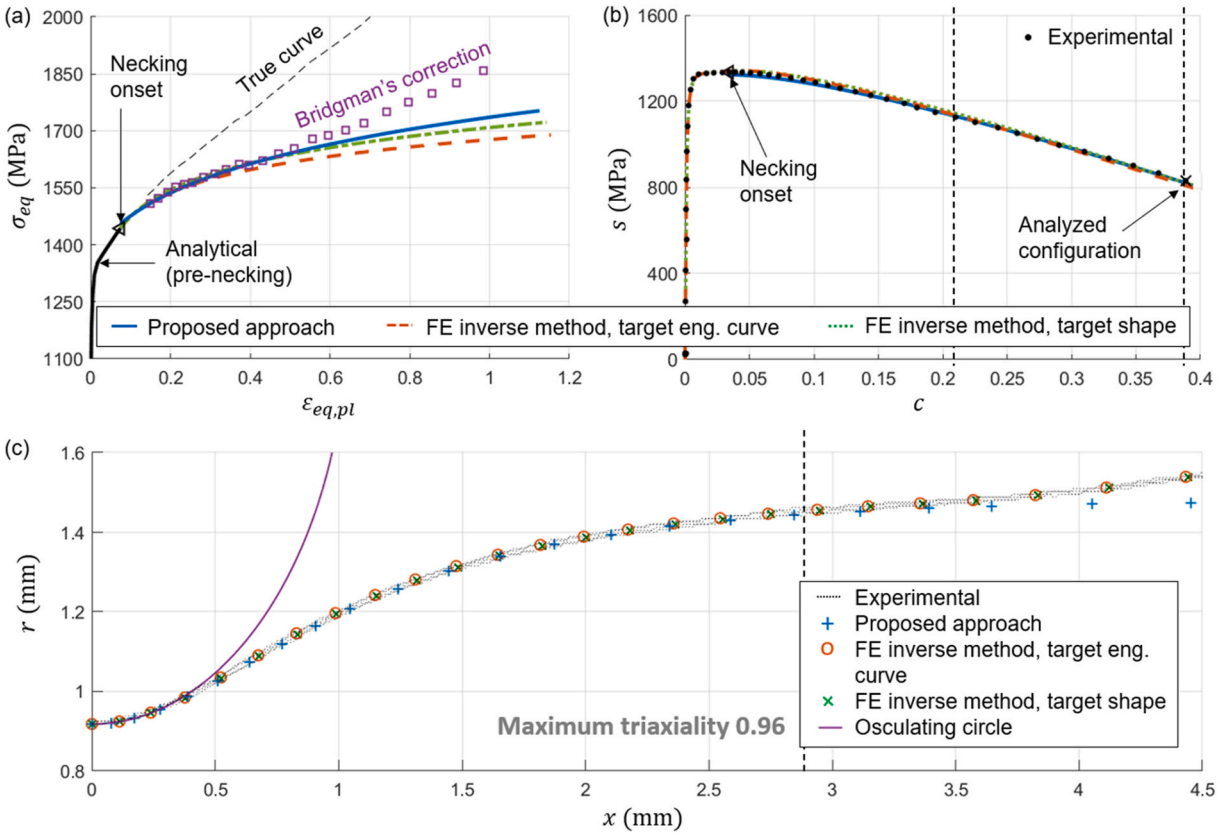

Fig. 10. Experimental results of 17-4 PH, in terms of (a) plastic flow curve, (b) engineering curve (in terms of engineering stress $s = F/A_0$ and radial engineering strain $c = |\Delta R|/R_0$), (c) specimen profile, in comparison with the numerical prediction obtained from different identification strategies.

catch a saturating behavior too. Nevertheless, the method would still be applicable to a wider database, enriched with other hardening models.

CRediT authorship contribution statement

Marta Beltramo: Writing – review & editing, Writing – original draft, Visualization, Software, Methodology, Investigation, Formal analysis, Data curation, Conceptualization. **Martina Scapin:** Writing – review & editing, Writing – original draft, Visualization, Validation, Supervision, Software, Resources, Project administration, Methodology, Investigation, Funding acquisition, Formal analysis, Data curation, Conceptualization. **Lorenzo Peroni:** Writing – review & editing, Writing – original draft, Visualization, Validation, Supervision, Software, Resources, Project administration, Methodology, Investigation, Funding acquisition, Formal analysis, Data curation, Conceptualization.

Declaration of competing interest

The authors declare that they have no known competing financial interests or personal relationships that could have appeared to influence the work reported in this paper.

Data availability

Data will be made available on request.

Appendix A. Comparing the specimen profile of materials with different uniform deformation

Consider two cylinders, denoted as 1 and 2, with different initial diameter D_0 and made of materials with different hardening laws, each characterized by its own ε_n at the necking onset. During the post-necking phase, the deformation localizes, so the diameter far from the neck will remain almost equal to D_n. Therefore, to compare the necking shape of cylinder 2 with the necking shape of cylinder 1, it would be necessary to scale the profile of cylinder 2 with a coefficient k_g as if at the necking onset it had a diameter $\widetilde{D}_{n2}$ equal to D_{n1}: $\widetilde{D}_{n2} = D_{n2}/k_g$; $\widetilde{D}_{n2} = D_{n1}$.

Thus, the expression of such coefficient can be written as $k_g = D_{n2}/\widetilde{D}_{n2} = D_{n2}/D_{n1}$.

Considering that until necking onset it holds: $\varepsilon = 2\ln\left(\frac{D_0}{D}\right)$, it results that:

$$k_g = \frac{D_{02}}{D_{01}} \exp\left(\frac{\varepsilon_{n1} - \varepsilon_{n2}}{2}\right). \tag{A.1}$$

From a practical point of view, within the identification procedure, the coefficient k_g is optimized for each profile of the database (instead of using Eq. A.1). The reason was to avoid uncertainties on the necking onset to affect the coefficient k_g. In case the initial gauge diameter of the specimen is the same as the cylinder of the database and $\varepsilon_{n,db} = \varepsilon_n$, it would not be necessary to scale the profile, and the algorithm would automatically find $k_g \approx 1$.

Appendix B. Comparing the engineering curve of materials with different uniform deformation

Consider two cylinders, denoted as 1 and 2, with different initial diameter D_0 and made of materials with different hardening laws, each characterized by its own ε_n at the necking onset. The aim of this appendix is to explain how it is possible to modify the engineering curve $s - c$ to remove the effect of uniform deformation, being the radial engineering strain $c = \frac{R_0 - R}{R_0} = 1 - \frac{R}{R_0} = 1 - \frac{D}{D_0}$.

It may be useful to explicitly consider the radial engineering strain at the necking onset:

$$c_n = 1 - \frac{D_n}{D_0},$$

$$c = 1 - \frac{D}{D_n}\frac{D_n}{D_0} = 1 - \frac{D}{D_n}(1 - c_n)\,.$$

By defining a "modified" radial engineering strain as $c^* = 1 - D/\mathrm{D}_n$, it results that:

$$c = 1 - (1 - c^*)(1 - c_n). \tag{B.1}$$

Moreover, it can be easily observed that the "modified" radial engineering strains c_1^* and c_2^* are directly comparable. Indeed, they coincide when $D_1/D_{1n} = D_2/D_{2n}$, which is consistent with the idea of removing the effect of a different uniform deformation.

Such "modified" radial engineering strains could be determined from c as:

$$c^* = 1 - \frac{1 - c}{1 - c_n} = \frac{\mathrm{c\text{-}c_n}}{\mathrm{1\text{-}c_n}}\,. \tag{B.2}$$

It is then possible to see how c_2 must be modified into $\widetilde{c}_2$ to become comparable with c_1 by plugging Eq. B.2 into Eq. B.1:

$$c_1 = 1 - (1 - c^*)(1 - c_{n1}) = 1 - \frac{1 - c_2}{1 - c_{n2}}(1 - c_{n1}) = 1 - (1 - c_2)\frac{1 - c_{n1}}{1 - c_{n2}}\,.$$

Therefore:

$$\widetilde{c}_2 = 1 - (1 - c_2)\frac{1 - c_{n1}}{1 - c_{n2}}. \tag{B.3}$$

This means that taking from the engineering curve the values of c_n is then possible to "correct" c_2.

In addition, it can be proved that such correction theoretically depends on the different uniform deformation and initial diameter. To this aim, consider that the term $\frac{1-c_{n1}}{1-c_{n2}}$ can be further expressed as:

$$\frac{1 - c_{n1}}{1 - c_{n2}} = \frac{D_{n1}/D_{01}}{D_{n2}/D_{02}} = \exp\left(\frac{\varepsilon_{n2} - \varepsilon_{n1}}{2}\right) = \frac{1}{k_g}\frac{D_{02}}{D_{01}}\,. \tag{B.4}$$

For what the engineering stress is concerned, it should be considered that, during uniform deformation, the same axial stress at a different axial strain gives a different force. Indeed, the same axial stress would be distributed on a different cross-section.

Considering the same two cylinders as before, it holds that before the necking onset:

$$s = \frac{F}{A_0} = \frac{\sigma A}{A_0} = \sigma\left(\frac{D}{D_0}\right)^2$$

and, to obtain $\widetilde{s}_2$ comparable with s_1, the scale coefficient k_g should be taken into account:

$$\widetilde{s}_2 = \sigma_2\left(\frac{\widetilde{D}_2}{D_{02}}\right)^2 = \sigma_2\left(\frac{D_2/k_g}{D_{02}}\right)^2 = \sigma_2\left(\frac{D_2}{D_{02}}\right)^2\frac{1}{k_g^2} = \frac{s_2}{k_g^2}.$$

Considering Eq. B.4, $\widetilde{s}_2$ can be also written as:

$$\widetilde{s}_2 = \frac{s_2}{k_g^2} = s_2\left(\frac{D_{01}}{D_{02}}\,\frac{1 - c_{n1}}{1 - c_{n2}}\right)^2. \tag{B.5}$$

From a practical point of view, within the identification procedure, Eq. B.3 and Eq. B.5 are used.

References

Beltramo, M., Scapin, M., Peroni, L., 2023. An advanced post-necking analysis methodology for elasto-plastic material models identification. Mater. Des. 230, 111937.

Bridgman, P.W., 1952. Studies in large plastic flow and fracture. In: Metallurgy and Metallurgical Engineering Series. McGraw Hill, New York.

Coppieters, S., Kuwabara, T., 2014. Identification of post-necking hardening phenomena in ductile sheet metal. Exp. Mech. 54, 1355–1371.

Coppieters, S., Cooreman, S., Sol, H., Van Houtte, P., Debruyne, D., 2011. Identification of the post-necking hardening behaviour of sheet metal by comparison of the internal and external work in the necking zone. J. Mater. Process. Technol. 211 (3), 545–552.

Coppieters, S., Sumita, S., Yanaga, D., Denys, K., Debruyne, D., Kuwabara, T., 2016. Identification of post-necking strain hardening behavior of pure titanium sheet. In: Residual Stress, Thermomechanics & Infrared Imaging, Hybrid Techniques and Inverse Problems, Volume 9: Proceedings of the 2015 Annual Conference on Experimental and Applied Mechanics. Springer International Publishing, pp. 59–64.

Defaisse, C., Mazière, M., Marcin, L., Besson, J., 2018. Ductile fracture of an ultra-high strength steel under low to moderate stress triaxiality. Eng. Fract. Mech. 194, 301–318.
Dunand, M., Mohr, D., 2010. Hybrid experimental–numerical analysis of basic ductile fracture experiments for sheet metals. Int. J. Solid Struct. 47 (9), 1130–1143.
Dunand, M., Mohr, D., 2011. On the predictive capabilities of the shear modified Gurson and the modified Mohr–Coulomb fracture models over a wide range of stress triaxialities and Lode angles. J. Mech. Phys. Solid. 59 (7), 1374–1394.
Dunnett, T., Balint, D., MacGillivray, H., Church, P., Gould, P., 2012. Scale effects in necking. In: EPJ Web of Conferences, 26. EDP Sciences, 01008.
Fu, J., Barlat, F., Kim, J.H., Pierron, F., 2017. Application of the virtual fields method to the identification of the homogeneous anisotropic hardening parameters for advanced high strength steels. Int. J. Plast. 93, 229–250.
Gromada, M., Mishuris, G., Öchsner, A., 2011. Correction Formulae for the Stress Distribution in Round Tensile Specimens at Neck Presence. Springer Science & Business Media.
Gross, A.J., Ravi-Chandar, K., 2015. On the extraction of elastic–plastic constitutive properties from three-dimensional deformation measurements. J. Appl. Mech. 82 (7), 071013.
Guo, Z., Bai, R., Lei, Z., Jiang, H., Liu, D., Zou, J., Yan, C., 2021. CPINet: parameter identification of path-dependent constitutive model with automatic denoising based on CNN-LSTM. Eur. J. Mech. Solid. 90, 104327.
Gupta, M.K., Singh, N.K., 2021. Post necking behaviour and hardening characterization of mild steel. Solid State Phenom. 319, 7–12.
Hutchinson, J.W., Miles, J.P., 1974. Bifurcation analysis of the onset of necking in an elastic/plastic cylinder under uniaxial tension. J. Mech. Phys. Solid. 22 (1), 61–71.
Kajberg, J., Lindkvist, G., 2004. Characterisation of materials subjected to large strains by inverse modelling based on in-plane displacement fields. Int. J. Solid Struct. 41 (13), 3439–3459.
Karniadakis, G.E., Kevrekidis, I.G., Lu, L., Perdikaris, P., Wang, S., Yang, L., 2021. Physics-informed machine learning. Nature Reviews Physics 3 (6), 422–440.
Kim, J.H., Serpantié, A., Barlat, F., Pierron, F., Lee, M.G., 2013. Characterization of the post-necking strain hardening behavior using the virtual fields method. Int. J. Solid Struct. 50 (24), 3829–3842.
Koch, D., Haufe, A., 2019. First Steps towards Machine-Learning Supported Material Parameter Identification.
La Rosa, G., Risitano, A., Mirone, G., 2003. Postnecking elastoplastic characterization: degree of approximation in the Bridgman method and properties of the flow-stress/true-stress ratio. Metall. Mater. Trans. 34, 615–624.
Li, X., Roth, C.C., Mohr, D., 2019. Machine-learning based temperature-and rate-dependent plasticity model: application to analysis of fracture experiments on DP steel. Int. J. Plast. 118, 320–344.
Li, Y., Zhang, Y., Li, S., 2021. Viscoplastic constitutive modeling of boron steel under large strain conditions and its application in hot semi-cutting. J. Manuf. Process. 66, 532–548.
Liu, Y., Zhao, T., Ju, W., Shi, S., 2017. Materials discovery and design using machine learning. Journal of Materiomics 3 (3), 159–177.
Marques, A., Pereira, A., Ribeiro, B., Prates, P.A., 2022. On the identification of material constitutive model parameters using machine learning algorithms. Key Eng. Mater. 926, 2146–2153.
Marth, S., Häggblad, H.Å., Oldenburg, M., Östlund, R., 2016. Post necking characterisation for sheet metal materials using full field measurement. J. Mater. Process. Technol. 238, 315–324.
Meißner, P., Watschke, H., Winter, J., Vietor, T., 2020. Artificial neural networks-based material parameter identification for numerical simulations of additively manufactured parts by material extrusion. Polymers 12 (12), 2949.
Meißner, P., Winter, J., Vietor, T., 2022. Methodology for neural network-based material card calibration using LS-DYNA MAT_187_SAMP-1 considering failure with GISSMO. Materials 15 (2), 643.
Mirone, G., 2004. A new model for the elastoplastic characterization and the stress–strain determination on the necking section of a tensile specimen. Int. J. Solid Struct. 41 (13), 3545–3564.
Mirone, G., Corallo, D., 2010. A local viewpoint for evaluating the influence of stress triaxiality and Lode angle on ductile failure and hardening. Int. J. Plast. 26 (3), 348–371.
Murata, M., Yoshida, Y., Nishiwaki, T., 2018. Stress correction method for flow stress identification by tensile test using notched round bar. J. Mater. Process. Technol. 251, 65–72.
Park, J.S., Kim, J.M., Barlat, F., Lim, J.H., Pierron, F., Kim, J.H., 2021. Characterization of dynamic hardening behavior at intermediate strain rates using the virtual fields method. Mech. Mater. 162, 104101.
Peroni, L., Scapin, M., 2018. Strength model evaluation based on experimental measurements of necking profile in ductile metals. In: EPJ Web of Conferences, 183. EDP Sciences, 01015.
Peroni, L., Scapin, M., Fichera, C., 2015. An advanced identification procedure for material model parameters based on image analysis. In: 10th European LS-DYNA Conference in Würzburg *(Germany)*.
Pham, Q.T., Nguyen-Thoi, T., Ha, J., Kim, Y.S., 2021. Hybrid fitting-numerical method for determining strain-hardening behavior of sheet metals. Mech. Mater. 161, 104031.
Rösler, J., Harders, H., Bäker, M., 2007. Mechanical Behaviour of Engineering Materials: Metals, Ceramics, Polymers, and Composites. Springer Science & Business Media.
Rossi, M., Lattanzi, A., Barlat, F., Kim, J.H., 2022. Inverse identification of large strain plasticity using the hydraulic bulge-test and full-field measurements. Int. J. Solid Struct. 242, 111532.
Roy, B.K., Korkolis, Y.P., Arai, Y., Araki, W., Iijima, T., Kouyama, J., 2022. Plastic deformation of AA6061-T6 at elevated temperatures: experiments and modeling. Int. J. Mech. Sci. 216, 106943.
Saje, M., Pan, J., Needleman, A., 1982. Void nucleation effects on shear localization in porous plastic solids. Int. J. Fract. 19, 163–182.
Scapin, M., Peroni, L., Fichera, C., 2014. Investigation of dynamic behaviour of copper at high temperature. Mater. A. T. High. Temp. 31 (2), 131–140.
Scapin, M., Beltramo, M., 2024. A Methodology for Post-Necking Analysis in Isotropic Metals. Metals 14 (5), 593.
Scapin, M., Peroni, L., Carra, F., 2016. Investigation and mechanical modelling of pure molybdenum at high strain-rate and temperature. Journal of Dynamic Behavior of Materials 2, 460–475.
Scapin, M., Peroni, L., Torregrosa, C., Perillo-Marcone, A., Calviani, M., 2019. Effect of strain-rate and temperature on mechanical response of pure tungsten. Journal of Dynamic Behavior of Materials 5, 296–308.
Scheider, I., Brocks, W., Cornec, A., 2004. Procedure for the determination of true stress-strain curves from tensile tests with rectangular cross-section specimens. J. Eng. Mater. Technol. 126 (1), 70–76.
Schmidt, J., Marques, M.R., Botti, S., Marques, M.A., 2019. Recent advances and applications of machine learning in solid-state materials science. npj Comput. Mater. 5 (1), 83.
Stoll, A., Benner, P., 2021. Machine learning for material characterization with an application for predicting mechanical properties. GAMM-Mitteilungen 44 (1), e202100003.
Tu, S., Ren, X., He, J., Zhang, Z., 2020. Stress–strain curves of metallic materials and post-necking strain hardening characterization: a review. Fatig. Fract. Eng. Mater. Struct. 43 (1), 3–19.
Tvergaard, V., Needleman, A., 1984. Analysis of the cup-cone fracture in a round tensile bar. Acta Metall. 32 (1), 157–169.
Wagner, N., Rondinelli, J.M., 2016. Theory-guided machine learning in materials science. Frontiers in Materials 3, 28.
Wang, L., Tong, W., 2015. Identification of post-necking strain hardening behavior of thin sheet metals from image-based surface strain data in uniaxial tension tests. Int. J. Solid Struct. 75, 12–31.
Yao, Z., Wang, W., 2022. Full-range strain-hardening behavior of structural steels: experimental identification and numerical simulation. J. Constr. Steel Res. 194, 107329.
Yu, R., Li, X., Yue, Z., Li, A., Zhao, Z., Wang, X., et al., 2022. Stress state sensitivity for plastic flow and ductile fracture of L907A low-alloy marine steel: from tension to shear. Mater. Sci. Eng., A 835, 142689.
Zeng, X., Huo, J.S., 2023. Rate-dependent constitutive model of high-strength reinforcing steel HTRB600E in tension. Construct. Build. Mater. 363, 129824.
Zhang, Z.L., Hauge, M., Ødegård, J., Thaulow, C., 1999. Determining material true stress–strain curve from tensile specimens with rectangular cross-section. Int. J. Solid Struct. 36 (23), 3497–3516.
Zhang, H., Coppieters, S., Jiménez-Peña, C., Debruyne, D., 2019. Inverse identification of the post-necking work hardening behaviour of thick HSS through full-field strain measurements during diffuse necking. Mech. Mater. 129, 361–374.
Zhang, C., Lou, Y., Zhang, S., Clausmeyer, T., Tekkaya, A.E., Fu, L., Chen, Q., Zhang, Q., 2021. Large strain flow curve identification for sheet metals under complex stress states. Mech. Mater. 161, 103997.
Zhang, H., Xu, C., Gao, T., Li, X., Song, H., 2023. Identification of strain hardening behaviors in titanium alloys using tension tests and inverse finite element method. J. Mech. Sci. Technol. 37 (7), 3593–3599.
Zhao, K., Wang, L., Chang, Y., Yan, J., 2016. Identification of post-necking stress–strain curve for sheet metals by inverse method. Mech. Mater. 92, 107–118.
Zhu, L., Huang, X., Liu, H., 2022. Study on constitutive model of 05Cr17Ni4Cu4Nb stainless steel based on quasi-static tensile test. J. Mech. Sci. Technol. 36 (6), 2871–2878.